The Journal of Chemical Physics

RESEARCH ARTICLE | NOVEMBER 22 2024

Anomalous pressure–density relations and speed of sound in bubbly water systems

Special Collection: Molecular Dynamics, Methods and Applications 60 Years after Rahman

Jesse L. Prelesnik ; Jingyi L. Chen ; Krishnan Mahesh ; J. Ilja Siepmann

Check for updates

J. Chem. Phys. 161, 204501 (2024)
https://doi.org/10.1063/5.0235457

View Online
Export Citation

Articles You May Be Interested In

KoopmanLab: Machine learning for solving complex physics equations

APL Mach. Learn. (September 2023)

Experimental realization of a quantum classification: Bell state measurement via machine learning

APL Mach. Learn. (September 2023)

22 November 2024 13:32:09

AIP Publishing

The Journal of Chemical Physics

Special Topics Open for Submissions

Learn More

AIP Publishing

The Journal of Chemical Physics ARTICLE pubs.aip.org/aip/jcp

Anomalous pressure–density relations and speed of sound in bubbly water systems

Cite as: J. Chem. Phys. 161, 204501 (2024); doi: 10.1063/5.0235457
Submitted: 27 August 2024 • Accepted: 4 November 2024 •
Published Online: 22 November 2024

View Online Export Citation CrossMark

Jesse L. Prelesnik,[1] Jingyi L. Chen,[1] Krishnan Mahesh,[2,a)] and J. Ilja Siepmann[1,3,b)]

AFFILIATIONS

[1] Department of Chemistry and Chemical Theory Center, University of Minnesota, 207 Pleasant Street SE, Minneapolis, Minnesota 55455-0431, USA
[2] Department of Aerospace Engineering and Mechanics, University of Minnesota, 110 Union Street SE, Minneapolis, Minnesota 55455-0153, USA
[3] Department of Chemical Engineering and Materials Science, University of Minnesota, 412 Washington Avenue SE, Minneapolis, Minnesota 55455-0132, USA

Note: This paper is part of the JCP Special Topic on Molecular Dynamics, Methods and Applications 60 Years after Rahman.
[a)] **Present address:** Naval Architecture and Marine Engineering, University of Michigan, 2600 Draper Drive, Ann Arbor, MI 48109, USA.
[b)] **Author to whom correspondence should be addressed:** siepmann@umn.edu

ABSTRACT

The speed of sound in bubbly water is an important parameter in the wave equations governing pressure–density relations for turbulent multi-phase flow simulations. Recent molecular simulation results indicate that, for bubbles that are thermodynamically stable at finite volume conditions, the derivative of total pressure P with density ρ has a negative sign, complicating the interpretation of the speed of sound. We show that such a negative compressibility is thermodynamically consistent in a single-component two-phase model at finite volume, and identify an empirically derived equation of state to illustrate that this observation is not an artifact of small simulation length scales. To reconcile this thermodynamic relation with measurements of sound propagation, we decompose the derivative $\partial P/\partial \rho$ for bubbly water into its constituent phases to identify absorptive and transmissive contributors, both with an equation of state and using molecular simulations. We find that the speed of sound in the liquid phase remains real-valued while the bubble attenuates sound, giving a negative system compressibility. The inclusion of N_2 molecules in molecular simulations illustrates that these observations are robust and hold also for mixtures. From these simulations, we also compute scattering functions for bubbly systems to identify oscillations associated with the speed of sound. Finally, the spherical harmonic modes of bubble oscillations are analyzed in the context of resonance with propagating waves.

Published under an exclusive license by AIP Publishing. https://doi.org/10.1063/5.0235457

22 November 2024 13:32:09

I. INTRODUCTION

The study of turbulent multi-phase flows is important for the field of oceanographic engineering, with applications such as noise reduction and mitigating damage to naval vessels.[1] These complex phenomena include a multitude of physicochemical driving forces that couple across broad time and length scales, presenting a considerable theoretical challenge.[2,3] At the forefront of modeling multi-phase flows is computational fluid dynamics (CFD), which solves transport equations numerically.[4,5] A prominent parameter in the wave equation is the speed of sound c, defined as $\sqrt{(\partial P/\partial \rho)_S}$, which describes the spatiotemporal behavior of pressure P perturbations as a function of density ρ. By nature, c is a real-valued scalar quantity in homogeneous systems.[6]

The pressure–density curve describing first-order vapor–liquid phase transitions is often modeled in thermodynamics using a van der Waals isotherm derived from perturbation theory, usually a cubic equation of state (EOS) that contains an inflection point for temperatures T below criticality.[7] To eliminate "unstable states" where $(\partial P/\partial \rho)_T \approx (\partial P/\partial \rho)_S < 0$, the Maxwell construction is usually imposed where a line of constant pressure connects densities on either side of the coexistence curve.[8] This interpretation is valid in the isobaric–isothermal and grand canonical ensembles, where systems at unstable points will collapse to either the homogeneous

Published under an exclusive license by AIP Publishing

liquid or vapor state, but in the canonical ensemble, this relaxation is impossible and a heterogeneous two-phase system is thermodynamically stable.[9–11] A major topic of discussion herein regards the assertion that there are regions where $\partial P/\partial\rho < 0$ for bubbly states in this ensemble and what consequences this has for wave propagation. It should be noted that CFD simulations usually involve cells of fixed volume.

Recent molecular simulation results in the canonical ensemble have indicated that, for a thermodynamically stable bubble in the absence of net flow, the pressure P (calculated via the virial theorem using the forces acting on the particles) varies with ρ such that $(\partial P/\partial\rho)_T < 0$.[11] The unusual sign of $(\partial P/\partial\rho)_T$ is mechanistically attributed to frustration in the liquid phase, which is less dense than at ambient conditions to reduce vapor–liquid interfacial tension. When the system density is lowered, the bubble grows resulting in the liquid being less stretched and the pressure increasing. This observation is consistent with the Young–Laplace equation, which was found by molecular simulation to be applicable to bubbles with a radius below 2 nm.[11] The negative sign of $(\partial P/\partial\rho)_T$ implies that c should be imaginary, however, which cannot straightforwardly be implemented in CFD simulations when voxels of finite volume are used to model the system. While the oceanographic literature ascribes real and imaginary components to c, the latter indicating attenuation,[12] it is unclear how a negative compressibility manifests as some real-valued speed of sound. Here we attempt to reconcile the negative compressibility in bubbly water with expectations about sound propagation and refute the claim that such a pressure–density relation is unphysical.

First, we provide some background thermodynamics and illustrate that a negative compressibility is consistent with the description of a single-component two-phase system at finite volume, a finding that is also in agreement with the Young–Laplace equation. We further present a numerical model for $P(\rho)$ based on a stiffened equation of state fitted to empirical pressure data in the homogeneous liquid, which is extended into the two-phase region by including self-consistent determinations of the liquid density (ρ_β) and pressure via the Young–Laplace equation. This model quantifies $(\partial P/\partial\rho)_T < 0$ and illustrates system size effects, explaining some apparent discrepancies between nanoscale molecular simulation and current experimental capabilities. The derivatives of several thermodynamic quantities are also available, allowing us to calculate $\partial P/\partial\rho_\beta$, which is interpreted as the speed of sound propagating through the liquid medium. Notably, it is a positive quantity. We then conduct molecular dynamics simulations to compute $(\partial P/\partial\rho)_S$ via direct thermodynamic relations to quantitatively validate the predictions of the EOS.

Finally, to provide broader context for these findings, we perform two separate analyses: (1) scattering functions are computed for homogeneous and bubbly water systems obtained from molecular dynamics simulations, where we show that characteristic oscillations corresponding to the speed of sound can still be identified in bubbly systems, and (2) a series of spherical harmonic basis functions are fitted to the bubble envelope on a frame-by-frame basis and time correlations are examined to assess whether the sound attenuating behavior of the bubble can be related to its fluctuations. Cumulatively, this work seeks to provide deeper physical insight into the nature of sound propagation in multi-phase systems.

II. METHODS

A. Thermodynamics of two-phase systems

We first introduce some simple conservative relations that will be referenced throughout, where particle number N and volume V are separated into constituent phases for the two-phase system with the vapor and liquid denoted by subscripts α and β, respectively. For simplicity, we limit to two phases and do not include a separate interfacial region:

$$V = V_\alpha + V_\beta, \tag{1a}$$

$$N = N_\alpha + N_\beta. \tag{1b}$$

For the bulk modulus of a single phase given by

$$K_\alpha = -V_\alpha \frac{\partial P}{\partial V_\alpha}, \tag{2}$$

Equation (1a) becomes

$$\frac{1}{K} = \frac{\alpha}{K_\alpha} + \frac{1-\alpha}{K_\beta}, \tag{3}$$

where we have defined the bubble volume fraction $\alpha = V_\alpha/V$ for brevity. It then follows that, from Eq. (1b),

$$\rho = \alpha\rho_\alpha + (1-\alpha)\rho_\beta. \tag{4}$$

A simple relation for $c(\alpha)$ can be found by combining Eqs. (3) and (4) as $c^2 = K/\rho$, where the densities and compressibilities of each phase are empirically determined constants and α varies. Doing so provides good agreement with experimental measurements with aqueous systems, where it is found that (real-valued) c decreases rapidly with α, dropping below c_{air} at $\alpha \approx 10^{-3}$.[6] The utility of this simple relation has justified its continued use in CFD, but we will show that K_α and K_β differ from their bulk values in a two-phase system such that the overall K given by Eq. (3) is negative.

To illustrate that $K < 0$ is thermodynamically consistent, we first restate an argument presented by Landau and Lifshitz,[13] where they meticulously showed that $(\partial P/\partial V)_S < 0$ and $(\partial P/\partial V)_T < 0$ for all homogeneous systems. We will then rephrase it in the context of a single-component two-phase system as done by Yang.[14] In the latter case, the inequality placed on $(\partial P/\partial V)_T$ is less restrictive, and when substitutions are made using parameter values for bubbly water, $(\partial P/\partial V)_T > 0$.

The argument posed by Landau and Lifshitz is based on the premise that a positive amount of work δW is needed to perturb a system from equilibrium. When this δW is applied to a homogeneous system, in any statistical mechanical ensemble, the relation

$$\delta U - T\delta S + P\delta V > 0 \tag{5}$$

holds. Following a Taylor expansion and some algebraic manipulations, they find the inequality can be rewritten as

$$\left[\frac{\partial^2 U}{\partial S^2}(\delta S)^2 + 2\frac{\partial^2 U}{\partial S \partial V}\delta S\delta V + \frac{\partial^2 U}{\partial V^2}(\delta V)^2\right] > 0. \tag{6}$$

22 November 2024 13:32:09

Published under an exclusive license by AIP Publishing

According to the principle of minimum energy, the second partial derivative test is applied to assert that $U(S,V)$ is about a minimum if and only if a set of inequalities hold, one of which being

$$\frac{\partial^2 U}{\partial V^2} > 0. \tag{7}$$

We can immediately see that Eq. (7) reduces to

$$\frac{\partial^2 U}{\partial V^2} = \frac{\partial}{\partial V}\left(\frac{\partial U}{\partial V}\right)_S = -\left(\frac{\partial P}{\partial V}\right)_S = K_S/V > 0. \tag{8}$$

Indeed, the adiabatic bulk modulus K_S in a homogeneous system must be positive. The same argumentation can be followed to show $K_T > 0$ as well. Now, we will reframe this argument for a heterogeneous system by once again perturbing the system from equilibrium by putting in work, thereby establishing an inequality, and then applying the second partial derivative test to break the inequality into sub-problems.

We follow the work of Yang,[14] wherein a spherical subsystem α with radius R is embedded in a bath β. They share an interface of area $4\pi R^2$ with a surface tension γ. The resulting energy expression contains explicit two-phase qualities, such as the chemical potential μ, as well as P and V terms for each phase. Yang has shown that when a system in equilibrium is perturbed in the canonical ensemble with Helmholtz free energy A,

$$\delta A = (\mu_\alpha - \mu_\beta)\delta N_\alpha - \left(P_\alpha - P_\beta - \frac{2\gamma}{R}\right)4\pi R^2 \delta R > 0 \tag{9}$$

holds when the interfacial region is negligibly thin. The analog to Eq. (6) is then

$$\left[\frac{\partial^2 A}{\partial N_\alpha^2}(\delta N_\alpha)^2 + 2\frac{\partial^2 A}{\partial N_\alpha \partial V_\alpha}\delta N_\alpha \delta V_\alpha + \frac{\partial^2 A}{\partial V_\alpha^2}(\delta V_\alpha)^2\right] > 0, \tag{10}$$

and three further inequalities arise according to the second partial derivative test. The important one here is that

$$\frac{\partial}{\partial V_\alpha}\left(\frac{\partial A}{\partial V_\alpha}\right)_T = \frac{-\partial\left(P_\alpha - P_\beta - \frac{2\gamma}{R}\right)}{\partial V_\alpha} > 0 \tag{11}$$

must be true. Note that the path of this derivative and those that follow are isothermal, as they arise from the Helmholtz free energy. Here we depart from the general formulation provided by Yang and interpret this condition in the context of bubbly water systems. To do this, we consider three terms:

$$-\frac{\partial P_\alpha}{\partial V_\alpha} + \frac{\partial P_\beta}{\partial V_\alpha} + \frac{\partial(2\gamma/R)}{\partial V_\alpha} > 0. \tag{12}$$

Previous molecular simulations[11] have demonstrated that γ for water is approximately linear with $1/R$ down to the nanoscale. Under this relationship, with γ_∞ the surface tension in the planar limit, the third term in Eq. (12) can be reduced to $(-2/3)(1/RV_\alpha)(2\gamma - \gamma_\infty)$. This quantity is thought to be strictly negative as the reduction in surface tension associated with bubble curvature is mild enough that $(2\gamma - \gamma_\infty) > 0$. The sum of the first two terms in Eq. (12) must then be positive. The first term is negligibly small compared to the second due to the small vapor pressure of water at near-ambient temperatures. Other authors have noted that P_β is approximately equal to the average pressure in the simulation,[15–17] such that

$$\frac{\partial P_\beta}{\partial V_\alpha} \approx \frac{\partial P}{\partial V_\alpha} > 0. \tag{13}$$

We then apply the chain rule, multiplying through $(\partial V_\alpha/\partial V)_N$, to finally reach $\partial P/\partial V$. Consequently, $\partial P/\partial V > 0$ if and only if $\partial V_\alpha/\partial V > 0$. Intuitively, this volume derivative states that the bubble volume will grow if the system is expanded at constant particle count, as has been observed in simulation.[11] Later sections of this manuscript will further demonstrate the truth value of this inequality.

Note the similarity between Eq. (11) and the Young–Laplace equation,

$$P_\alpha - P_\beta = \frac{2\gamma}{R}, \tag{14}$$

and so it is no surprise that this conclusion can be reached when Eq. (14) is used as a starting place instead. This is achieved by applying the same arguments such as $P_\alpha - P_\beta \approx -P$ and asserting that $\partial V_\alpha/\partial V > 0$. The result is again isothermal because the surface tension γ is a temperature-dependent quantity here held constant. Next, we will quantify these derivatives both using a macroscopic EOS and perform nanoscale molecular dynamics simulations to sample particle densities to quantify these volume (or density) derivatives.

B. Stiffened EOS with Young–Laplace

We now seek an expression for $P(\rho)$ in the bubbly two-phase region that will be amenable to arbitrary R, allowing several thermodynamic relations to be quantified. To begin, an empirical EOS has been determined to describe $c(\rho)$ in homogeneous liquid systems, parameterized as[18]

$$c = \left(\frac{\partial P}{\partial \rho}\right)_S^{1/2} \approx \left(\frac{\partial P}{\partial \rho}\right)_T^{1/2} = a_0 + a_1\rho + a_2\rho^2. \tag{15}$$

The parameters a_n are determined by fitting to measurements of c, determined by experiments to be $a_0 = 1.298 \times 10^4$, $a_1 = -2.667 \times 10^1$, and $a_2 = 1.519 \times 10^{-2}$, in units such that c is in (m/s) and ρ is in (kg/m^3). Integrating the square of this EOS gives

$$P = \int\left(a_0 + a_1\rho + a_2\rho^2\right)^2 \mathrm{d}\rho = a_0^2\rho + \frac{1}{3}(2a_0a_2 + a_1^2)\rho^3 + a_0a_1\rho^2 + \frac{1}{2}a_1a_2\rho^4 + \frac{1}{5}a_2^2\rho^5 + C, \tag{16}$$

where the constant of integration C is set such that $P(997.04\ \mathrm{kg/m^3}) = 101.325\ \mathrm{kPa}$,[19] giving $C = -3.442 \times 10^{10}$ Pa. To extend $P(\rho)$ to densities below its spinodal decomposition where the system enters the bubbly two-phase region, we utilize the Young–Laplace equation. We rewrite this relation with $P_\beta \to P$ and the radius R is replaced by an expression for volume. The bubble volume is αV, where α is expressed in terms of densities using Eq. (4):

$$P = P_\alpha - 2\gamma\left(\frac{3}{4\pi}V\frac{\rho_\beta - \rho}{\rho_\beta - \rho_\alpha}\right)^{-1/3}. \tag{17}$$

22 November 2024 13:32:09

Published under an exclusive license by AIP Publishing

The inclusion of V provides an explicit system-size dependence. Here we treat ρ_α as an empirical constant, 0.023 kg/m^3.[20] We use the experimental surface tension of $\gamma = 71.995$ mN/m,[21] and the saturated vapor pressure of $P_\alpha = 3.1$ kPa,[22] all at the target temperature of 298 K. Because these parameters are in general temperature-dependent but are here taken to be constants, all derivatives produced by this numerical procedure are explicitly isothermal. Then a solution for $P(\rho)$ and ρ_β is found iteratively, using Eq. (17) to self-consistently identify the homogeneously stretched density ρ_β at a given P. Repeating this process at many values of ρ gives sufficient information to evaluate interesting thermodynamic quantities like $\partial P/\partial \rho_\beta$, bulk moduli, and $\partial V_\alpha/\partial V$.

To adjust the density ρ, either N or V can be varied while the other is held constant. Unless otherwise specified, we choose to hold V constant for analyses contained herein because this highlights the system-size dependence explicitly contained within Eq. (17) and aligns with simulation setups from prior studies.[11] However, some quantities such as $(\partial V_\alpha/\partial V)_N$ are only defined at constant particle count, so the stiffened EOS with Young–Laplace is solved accordingly to study their behavior. In these cases, the value for V reported to discuss finite size effects is the volume set at $\rho = 800$ kg/m^3. In general, varying either N or V gives comparable results and key findings such that $(\partial P/\partial \rho) < 0$ are true in both scenarios.

If the empirical parameters provided to the stiffened EOS with Young–Laplace are chosen to be those determined from molecular simulation for a given force field rather than experiment, then the resulting $P(\rho)$ curve should quantitatively match simulation results for the speed of sound. The four coefficients of Eq. (16) are obtained by fitting to $P(\rho)$ data from molecular simulation for the homogeneous liquid. Prior work has shown that $P(\rho)$ is not subject to finite size effects in the homogeneous part, so system size is irrelevant for the fit.[11] Quantities like γ and ρ_α must be measured from simulation as well.

Before moving on, we comment on the expected behavior of $\partial V_\alpha/\partial V$, which is accessible analytically in the infinitely large bubble limit. In this limit, ρ_β approaches its saturated liquid density and is an empirical constant. Beginning with Eq. (4) and taking N as constant while V_α is a function of V, we evaluate

$$\frac{\partial \alpha}{\partial \rho} = \left(\frac{\partial [V_\alpha/V]}{\partial [N/V]}\right)_N = \frac{V_\alpha}{N} - \frac{V}{N}\frac{\partial V_\alpha}{\partial V}, \tag{18}$$

which can be rearranged as

$$\frac{\partial V_\alpha}{\partial V} = \alpha - \rho \frac{\partial \alpha}{\partial \rho}. \tag{19}$$

Identifying that $\partial \alpha/\partial \rho = (\rho_\alpha - \rho_\beta)^{-1}$ when ρ_α and ρ_β are treated as constants, we find

$$\left(\frac{\partial V_\alpha}{\partial V}\right)_N = \frac{\rho_\beta}{\rho_\beta - \rho_\alpha} > 1, \tag{20a}$$

$$\left(\frac{\partial V_\beta}{\partial V}\right)_N = \frac{-\rho_\alpha}{\rho_\beta - \rho_\alpha} < 0. \tag{20b}$$

It is interesting to note that $\partial V_\alpha/\partial V$ and $\partial V_\beta/\partial V$ have opposite signs. This implies that the bulk moduli of the two phases will have opposite signs as well. The negative value for K observed in bubbly water systems is owed entirely to K_α, which is also negative, while K_β remains positive. Even at small α, the anomalous behavior of the vapor phase dominates some important thermophysical properties.

The numerically solved stiffened EOS with Young–Laplace presented here is limited in that ρ_α is treated as constant, meaning that $\partial P/\partial \rho_\alpha$ is inaccessible through this approach. This relation will be revisited with molecular simulation.

C. Molecular simulations and bubble detection

Molecular dynamics simulations were conducted using two different water models, TIP4P/2005[23] and mW.[24] The former was selected due to its accurate reproduction of many thermodynamic properties of neat water, such as the enthalpy of vaporization, surface tension, and speed of sound, but not the saturated vapor pressure.[11] The latter is a coarse-grained single-site model lacking long-range interactions, which captures the structure of liquid water via three-body interactions. While its accuracy compared to experiment is modest,[11] the reduced computational cost allows for larger system sizes and longer simulation lengths with a larger number of particles.

All simulations were conducted in the canonical (NVT) ensemble at 298 K at densities spanning 800–1000 kg/m^3 with a Nosé–Hoover thermostat using a damping parameter of 100 time steps. Simulation time steps were 1.0 fs for TIP4P/2005 and 2.0 fs for mW. When determining thermophysical properties, simulation lengths were 10 and 50 ns, respectively, while for evaluating time correlations, the lengths were 2 ns. In each case, equilibration was performed for at least 1 ns. For the TIP4P/2005 model, the edge length L of the cubic simulation box was chosen to be 4, 6, or 8 nm, while for the mW model, L spanned 4, 8, or 16 nm, held constant while N varies to adjust ρ. The number of independent simulations started with different random number seeds performed for each system and state point, as a means of estimating uncertainties (e.g., standard error of the mean) from statistically independent measurements, varied from 8 to 48.

Following Chen *et al.*, no tail corrections were applied for the TIP4P/2005 model, and a larger Lennard-Jones cutoff of 14 Å was used.[11] The TIP4P/2005 model was simulated using the ms2 simulation software package version 4.0,[25] with the package's reaction field electrostatics for long-range interactions taking $\varepsilon_s = 10^{10}$ and a center-of-mass based cutoff. The ms2 package is advantageous for computing the speed of sound due to the thermodynamic information it provides as outputs, but the mW model is not yet implemented and so it was simulated using Large-scale Atomic/Molecular Massively Parallel Simulator (LAMMPS) 2020 instead.[26] Where applicable, nitrogen gas included in mW simulations was modeled using a force field specifically developed for use with mW water,[27] a single-site Lennard-Jones bead where the energy and its derivative smoothly taper to zero at a distance of 9 Å.

The boundaries of a vapor bubble are identified using the Willard–Chandler (WC) dividing surface.[28] For the time-dependent molecular density defined as

$$\rho(\mathbf{r}, t) = \sum_{i=1}^{N} \delta[\mathbf{r} - \mathbf{r}_i(t)], \tag{21}$$

22 November 2024 13:32:09

Published under an exclusive license by AIP Publishing

where t is the time, $\mathbf{r}$ is a position vector, particles are indexed on i, and $\delta[\cdots]$ is the Dirac delta function, a 3D Gaussian kernel function with width parameter ξ is applied. We take ξ to be 2.4 Å, as has been used for water.[29] The Gaussian-smoothed density field is then

$$\tilde{\rho}(\mathbf{r},t) = (2\pi\xi^2)^{-3/2}\sum_{i=1}^{N} \exp\left(\frac{-|\mathbf{r}-\mathbf{r}_i(t)|^2}{2\xi^2}\right), \tag{22}$$

and an isosurface is drawn at a constant density of 0.016 Å^3,[28] approximately one half of the bulk liquid density at ambient conditions. The manifold was represented as a triangular mesh via the marching cubes algorithm[30] with 1 Å voxels. For a closed triangular mesh with normal vectors pointing outward, the volume V_α and center of mass $\mathbf{r}_c$ are computed analytically from a sum over triangles indexed on i, each containing three vertices $[[x_1,y_1,z_1],[x_2,y_2,z_2,],[x_3,y_3,z_3]]_i$, as[31]

$$V_\alpha = \frac{1}{6}\sum_i (-x_3y_2z_1 + x_2y_3z_1 + x_3y_1z_2 - x_1y_3z_2 - x_2y_1z_3 + x_1y_2z_3), \tag{23a}$$

$$\mathbf{r}_c = \frac{V_\alpha}{4}\sum_i [(x_1+x_2+x_3),(y_1+y_2+y_3),(z_1+z_2+z_3)]. \tag{23b}$$

This method for computing bubble properties is in close agreement with those reported by Chen *et al.*[11] with respect to bubble volume and anisotropy, as illustrated in Sec. III. The two simulation approaches are compared with the above stiffened EOS with Young–Laplace to provide a robust picture of bubble volume–density relationships.

Calculating the vapor density is particularly challenging from these simulations. It is imperative that interfacial water molecules are not counted toward the vapor because doing so produces estimated orders of magnitude larger than the known saturated vapor density used in the EOS with Young–Laplace. Furthermore, the low vapor pressure of water leads to very few molecules occupying the bubble region, giving poor statistics. Therefore, the vapor density was measured using a spherical subvolume centered in the bubble with a radius 5 Å less than the bubble radius. For consistency, the liquid density was obtained using the subvolume outside the bubble with the same delta. Prior works have measured the liquid density by fitting radial density profiles to a sigmoid function[11] but this strategy provided unreliable results for the vapor density.

D. Calculation of the speed of sound

Because single-component two-phase systems are unstable in the isobaric–isothermal (NPT) ensemble, the speed of sound cannot be computed via the usual fluctuation relations in V. Instead, the speed of sound was computed via direct thermodynamic relations as provided by Lustig.[32] This method has been discussed in detail elsewhere, and so only an overview of key concepts is provided here. The Helmholtz free energy A is related to the canonical partition function Q via

$$A(N,V,T) = -k_\mathrm{B}T\ \ln\ Q(N,V,T). \tag{24}$$

Any thermodynamic property can be obtained from some combination of partial derivatives of A or ln Q. Particularly, the derivatives with respect to V and $1/k_\mathrm{B}T$ are defined as

$$\frac{\partial^{m+n}(A/k_\mathrm{B}T)}{\partial^m(1/k_\mathrm{B}T)\partial V^n} \equiv \mathscr{A}_{mn} \tag{25}$$

for positive integers m, n. The functions $\mathscr{A}_{mn}$ can be expressed in terms of volume derivatives $(\partial^i U/\partial V^i)_{T,N}$ for $i = 0, 1, 2$, as detailed extensively by Lustig.[33] A myriad of thermodynamic properties, including c^2, are then expressed in terms of $\mathscr{A}_{mn}$. The set of $\mathscr{A}_{mn}$ are computed natively within the ms2 software, and so are outputted by default for TIP4P/2005 simulations. The three-body mW model is not available in ms2, however, and so the volume derivatives $(\partial^i U/\partial V^i)_{T,N}$ are computed by post-processing LAMMPS trajectories. The mW potential[24] is given by summing over trios of particles i, j, and k, such that

$$U = \sum_i\sum_{j>i}\phi_2(r_{ij}) + \sum_i\sum_{j\neq i}\sum_{k>j}\phi_3(r_{ij},r_{ik},\theta_{ijk}) \tag{26}$$

for pairwise ϕ_2 and three-body ϕ_3. The derivative $\partial U/\partial V$ is obtained using a coordinate transformation and the chain rule. Real coordinates $\mathbf{r}$ that would scale as a function of changing V are represented in terms of fractional coordinates $\mathbf{r}'$ invariant with volume, such that $\mathbf{r}_i = V^{1/3}\mathbf{r}_i'$. Doing so allows the derivative $\partial r/\partial V$ to be used in conjunction with the analytically known $\partial U/\partial r$. That is, for $\partial r_{ij}/\partial V = r_{ij}/3V$, we have

$$\frac{\partial U}{\partial V} = \sum_i\sum_{j>i}\left[\frac{\partial\phi_2}{\partial r_{ij}}\frac{\partial r_{ij}}{\partial V}\right] + \sum_i\sum_{j\neq i}\sum_{k>j}\left[\frac{\partial\phi_3}{\partial r_{ij}}\frac{\partial r_{ij}}{\partial V} + \frac{\partial\phi_3}{\partial r_{ik}}\frac{\partial r_{ik}}{\partial V} + \frac{\partial\phi_3}{\partial\theta}\frac{\partial\theta}{\partial V}\right], \tag{27}$$

and because the simulation box is isotropic, $\partial\theta/\partial V = 0$. For brevity, the derivatives of type $\partial\phi/\partial r$ and the formula for the second derivative $\partial^2U/\partial V^2$ are presented in the supplementary material. With these formulae, $(\partial P/\partial\rho)_S = c^2$ can be computed for the mW model. Note that both the isentropic and isothermal moduli are available from this measuring prescription, and so a careful validation of the approximation $(\partial P/\partial\rho)_S \approx (\partial P/\partial\rho)_T$ can be performed for systems where this difference may be substantive.

The speed of sound can also be approximated in bubbly water systems via finite differences, giving $(\partial P/\partial\rho)_T$ in the canonical ensemble. We compare this quantity to the more direct measurement $(\partial P/\partial\rho)_S$ as a means of robustly demonstrating that this derivative is negative in bubbly water systems regardless of methodology or conditions. In this case, multiple independent simulations are run at slightly different densities (box edge length L adjusted by ±0.1 and ±0.05 Å) and the derivative estimated from a linear fit through their resulting averages. Uncertainties for the slope were obtained through a bootstrapping approach where the linear fit was performed at least four times and the standard error of the mean reported.

Note that the approximation $(\partial P/\partial\rho)_T \approx (\partial P/\partial\rho)_S$ is a peculiarity of liquid water and not universally applicable.[34] Future studies on chemical compounds other than water will have to examine this approximation on a case-by-case basis. We show that it is valid for our models in Sec. III B.

22 November 2024 13:32:09

Published under an exclusive license by AIP Publishing

E. Scattering functions

Scattering functions were computed using the dynasor module.[35] From the density relation given in Eq. (21), its spatial Fourier transform (FT) is given by

$$\rho(\mathbf{k},t) = \sum_{i=1}^{N} \exp\left[-i\mathbf{k}\cdot\mathbf{r}_i(t)\right]. \tag{28}$$

The intermediate scattering function $F(\mathbf{k},t)$ is then defined as[36]

$$F(\mathbf{k},t) = \frac{1}{N}\langle\rho(\mathbf{k},t)\rho(-\mathbf{k},0)\rangle \tag{29}$$

for $\mathbf{k} = (2\pi/L)[l,m,n]$, where L is the cubic box edge length and l,m,n are integers equal to or greater than zero. Partial scattering functions arise when the sum over N particles in Eq. (28) is over N_O oxygen or N_H hydrogen atoms, giving atomic Fourier densities $\rho_H(\mathbf{k},t)$ or $\rho_O(\mathbf{k},t)$. Equation (29) then corresponds to one of the combinations OO, HH, or OH, and the total $F(\mathbf{k},t)$ is a linear combination of these partial intermediate scattering functions. When replicating experimental scattering results, each atomic nucleus is assigned a scattering length that describes its interaction strength with the incoming beam. So as to make no declaration about the nature of the scattering experiment, whether it is conducted with electrons or neutrons, for example, we weight the functions $F_{OO}(\mathbf{k},t)$, $F_{OH}(\mathbf{k},t)$, and $F_{HH}(\mathbf{k},t)$ with weights 1, 2, and 1, respectively. The qualitative features for each partial scattering function are similar.

The dynamic structure factor $S(\mathbf{k},\omega)$ is the temporal FT of $F(\mathbf{k},t)$,

$$S(\mathbf{k},\omega) = \frac{1}{2\pi}\int_{-\infty}^{\infty} F(\mathbf{k},t)\exp(-i\omega t)\mathrm{d}t. \tag{30}$$

The speed of sound can be extracted from either F or S in a variety of ways. In what follows, only the modulus $|\mathbf{k}| = k$ is important. If distinct peaks are present in $S(k,\omega)$, one can extract c by identifying the frequency $\omega_s(k)$ of the first nonzero peak in $S(k,\omega)$ and plot as a function of k to extrapolate to zero wavevector. We will see, however, that identifying these peaks from local maxima is challenging in bubbly water applications. An alternative approach is that analytical functions can be fit to data, and c extracted from the fit. For $F(k,t)$, the fit function is[37]

$$\frac{F(k,t)}{F(k,0)} = \frac{\varepsilon-1}{\varepsilon}\exp(-D_T k^2 t) + \frac{1}{\varepsilon}\exp(-\Gamma k^2 t)[\cos(ckt) + b(k)\sin(ckt)], \tag{31}$$

where ε is the ratio of specific heats C_P/C_V, D_T is the thermal diffusivity, Γ is the sound attenuation coefficient, and $b(k)$ is given by $[\Gamma + D_T(\varepsilon-1)]k/c$. The inclusion of a sine term in Eq. (31) is justified in Schoen *et al.*[37] using a derivation to low-order in k. A corresponding fit function for $S(k,\omega)$ is the real part of the temporal FT of Eq. (31), but fitting data to $F(k,t)$ was found to be more reliable. This is because $\mathrm{FT}(\sin(x))$ is wholly imaginary, and so this term is dropped when fitting to $S(k,\omega)$.

Once a series of $c(k)$ have been identified at different wavevectors, a hydrodynamic relation can sometimes be used to extrapolate to $c(0)$.[37,38] Strong coupling between hydrodynamic modes results in anomalous dispersion, however, and we find its functional form inappropriate for describing our data.

F. Spherical harmonics

To further quantify molecular mechanisms relating to sound attenuation, we sought to identify time scales associated with bubble undulations. The triangular mesh describing the bubble interface was fitted to spherical harmonic basis functions in a manner akin to the Fourier series, allowing autocorrelation functions to be extracted for each mode. A smooth manifold f can be approximated in the following form:[39]

$$f(\theta,\phi) \approx \sum_{l=0}^{l_{\max}}\sum_{m=-1}^{l} a_m^l Y_m^l(\theta,\phi), \tag{32}$$

where θ and ϕ are the polar and azimuth angles in spherical coordinates and $Y_m^l(\theta,\phi)$ is a spherical harmonic function of order l and degree m with $|m| \le l$, and a_m^l is a weighting coefficient. The spherical harmonics were described as a combination of associated Legendre polynomials, $P_m^l(\cos\theta)$.

The coefficients a_m^l are solved by inverting Eq. (32), which are the amplitudes necessary to reproduce the manifold describing the bubble boundary. Prior to the spherical harmonic fitting process, the origin was set to the bubble center. For computational efficiency, the largest l coefficient considered was $l = 6$. See Nortje *et al.*[39] for additional technical discussion, including Tikhonov regularization parameters and the algorithm for determining the needed weights a_m^l.

III. RESULTS AND DISCUSSION

A. Stiffened EOS with Young–Laplace

We first demonstrate agreement between Eq. (17) and molecular simulation data, using either the mW or TIP4P/2005 model. The cubic polynomial coefficients for Eq. (16) were re-fit to describe the homogeneous $P(\rho)$ region from Chen *et al.*[11] at constant volume. For the mW model, these coefficients are $a_0 = 1.60\times10^4$, $a_1 = -4.07\times10^1$, $a_2 = 2.70\times10^{-2}$, and $C = -4.13\times10^{10}$, in units evaluating to Pa and kg/m^3. For the TIP4P/2005 model, these parameters are $a_0 = 1.45\times10^4$, $a_1 = -3.10\times10^1$, $a_2 = 1.79\times10^{-2}$, and $C = -4.13\times10^{10}$.

The behavior of $P(\rho)$ in the bubbly region is computed numerically at constant V, and then overlaid with simulation data in Fig. 1. The excellent agreement between simulation and the EOS in the bubbly region is attributed to the Young–Laplace equation being upheld even at the nanometer scale.[11] The near-quantitative accuracy of the EOS with simulation data validates the assumptions made therein and supports its further use, both on length scales larger than accessible to simulation and to compute other properties like $(\partial P/\partial\rho_\beta)_T$. Interestingly, the bubbly and homogeneously stretched branches of the stiffened EOS with Young–Laplace meet at densities that increase with system size and that correspond to bubble radii consistent with the smallest bubble size observable in simulations.[11] As noted previously, addition of nitrogen at a mole fraction of 0.001 does not significantly alter the $p(\rho)$ curve.

22 November 2024 13:32:09

Published under an exclusive license by AIP Publishing

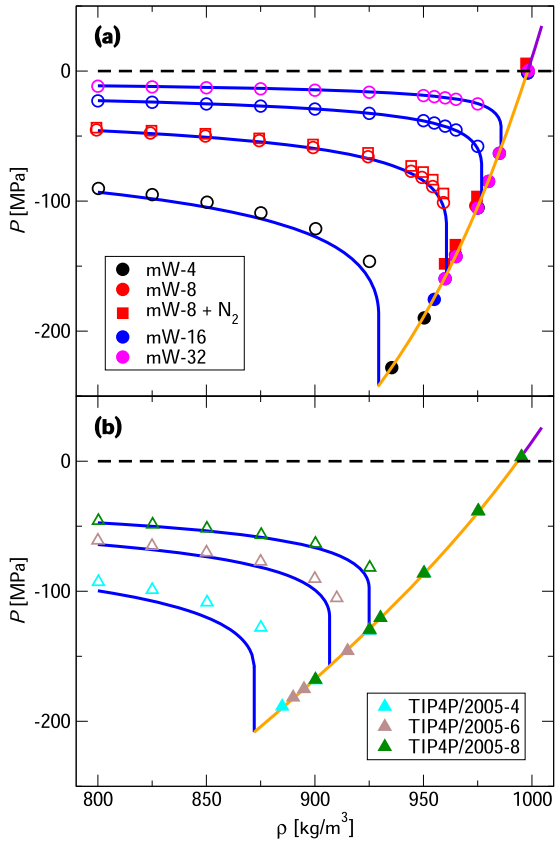

FIG. 1. Comparison between numerical results using the stiffened EOS with Young–Laplace at constant V (lines) with molecular simulation results from Chen *et al.*[11] (symbols) for two water models: (a) mW and (b) TIP4P/2005, all at 298 K. Parameters for the stiffened EOS were fit from the homogeneous simulation data. A horizontal dashed black line indicates the saturated vapor pressure P_{sat} of the water model. The compressed liquid above P_{sat} is purple and the homogeneously stretched liquid below is gold. Blue lines correspond to the bubbly region. Different symbol colors indicate simulations of different sizes, where the number that appears in the legend is the simulation box edge length L, in nm. Nitrogen gas was included with the mW model at a mole fraction of 0.001 and edge length L = 8 nm as indicated in red squares, as taken from Chen *et al.*[27]

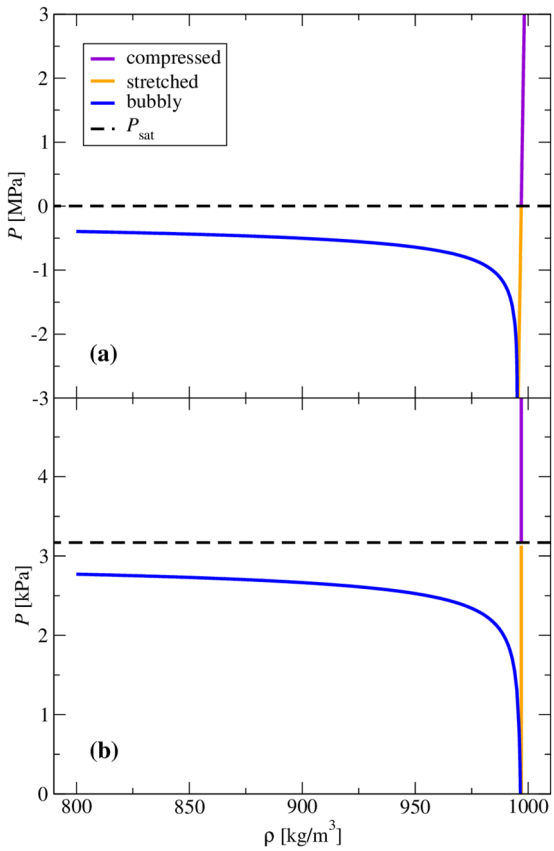

FIG. 2. Comparison of $P(\rho)$ results obtained from the stiffened EOS with Young–Laplace at constant V for two different system sizes (using experimental parameters as described in the text). With cell volume $V = L^3$, we show (a) L = 1 μm and (b) L = 1 mm. Notice the different scales for the pressure. The branches meet at R = 76 nm and 24 μm for L = 1 μm and 1 mm, respectively.

We now switch to using experimental parameters for the stiffened EOS to provide a quantitative prediction for $P(\rho)$ on experimentally measurable length scales (Fig. 2). With increasing system volume $V = L^3$, we find that the bubbly part of $P(\rho)$ rises to approach P_{sat}. The curvature remains qualitatively similar in each case, although the line flattens as $L \to \infty$ to become arbitrarily close to P_{sat} across the range of ρ. Notably, for $L \gtrsim 1$ mm, the bubbly part of $P(\rho) > 0$, meaning that experimental pressure measurements of optically resolved bubbles should appear as positive values rather than the negative pressures predicted at the micron scale. For even smaller bubbles on the nanoscale, the negative pressures can exceed 100 MPa in magnitude. Most importantly, despite the curve flattening, we still find $\partial P/\partial\rho < 0$ for all finite L.

The EOS solution for $P(\rho)$ at constant N also provides access to $(\partial V_\alpha/\partial V)_N$ as a function of system size and density (Fig. 3). As predicted by Eq. (20a), in the infinite size limit, we see that $\partial V_\alpha/\partial V$ approaches a constant value given by $\rho_\beta^{sat}/(\rho_\beta^{sat} - \rho_\alpha^{sat})$, where the superscript on ρ indicates the saturated values for the liquid and vapor densities, 997.04 and 0.023 kg/m^3, respectively. At smaller system sizes, $\partial V_\alpha/\partial V$ is strictly greater than its asymptotic value, meaning that $\partial V_\alpha/\partial V$ is always greater than unity. Mechanistically, this means that the bubble volume grows by an amount greater than the increment in total system volume, which can only occur if the liquid simultaneously becomes denser. Indeed, this has been observed in molecular simulations.[11] The stated condition that $\partial V_\alpha/\partial V > 0$ is a requirement for $\partial P/\partial V > 0$ in thermodynamically stable systems is therefore satisfied according to this EOS.

When $V_\alpha + V_\beta = V$, the statement $\partial V_\alpha/\partial V > 1$ necessitates that $\partial V_\beta/\partial V < 0$, indicating that the liquid exhibits the behavior expected of a homogeneous phase, $\partial P/\partial V_\beta < 0$. This suggests that sound propagation persists in the liquid even while the total system derivatives have atypical signs. This is possible because the liquid forms a continuous network while the bubbles are isolated.

To better understand sound propagation in the liquid, we take the derivatives $\partial P/\partial\rho$ and $\partial P/\partial\rho_\beta$, which are accessible

22 November 2024 13:32:09

Published under an exclusive license by AIP Publishing

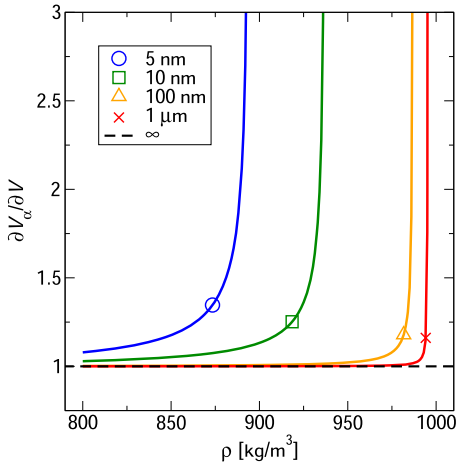

FIG. 3. Numerical solution for $(\partial V_\alpha/\partial V)_N$ as given by the stiffened EOS with Young–Laplace at constant N in the bubbly region for a variety of system sizes $V = L^3$: L = 5 nm (blue), L = 10 nm (green), L = 100 nm (gold), and L = 1 μm (red). In the infinite system size limit, $\partial V_\alpha/\partial V \to \rho_\beta^{sat}/(\rho_\beta^{sat} - \rho_\alpha^{sat})$, where the superscript on ρ denotes the saturated values for the liquid and vapor densities, 997.04 and 0.023 kg/m^3, respectively, as given by Eq. (20a).

numerically in this model. While $\partial P/\partial\rho$ is obviously negative in the bubbly region, as seen in Fig. 1, $\partial P/\partial\rho_\beta \equiv c_\beta^2 > 0$ and provides a real-valued speed of sound using experimental parameters (Fig. 4).

In the large bubble limit, $c_\beta(\rho)$ approaches $c(\rho_\beta^{sat})$, given by the model as 1491 m/s, which is in agreement with the recommended value of 1496 m/s.[40] For smaller bubbles, the $c_\beta(\rho)$ trace is curved, asymptotic to $c(\rho_\beta^{sat})$ at low densities and lower bounded by the homogeneously stretched $c(\rho)$ from the stiffened EOS. For bubbles with $R > 10$ nm, the maximum deviation from $c(\rho_\beta^{sat})$ is <1%,

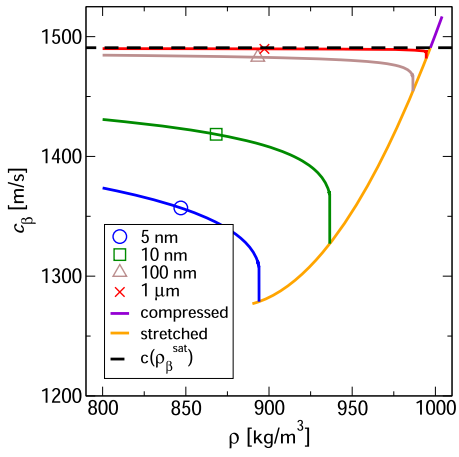

FIG. 4. Numerical values of $\sqrt{\partial P/\partial\rho_\beta}$ evaluated at constant V at four different system sizes, $V = L^3$: L = 5 nm (blue), L = 10 nm (green), L = 100 nm (brown), and L = 1 μm (red). The stiffened EOS is given in gold/purple, and the dashed black line marks c at ambient density, 997.04 kg/m^3.

indicating that using a constant c_β is an appropriate approximation in the large bubble limit. The observation that $\partial P/\partial\rho_\beta > 0$ and approaches the expected value of $c^2(\rho_{liq})$ further emphasizes that sound propagation through the fluid is still possible in bubbly systems despite the anomalous pressure–density relations at the system level.

B. Molecular simulation

The speed of sound was computed from simulation for the mW and TIP4P/2005 water models described using both direct thermodynamic relations, $(\partial P/\partial\rho)_S = c^2$ at single density points, and approximated using finite differences, $(\partial P/\partial\rho)_T \approx c^2$ (Fig. 5). Predictions made by the stiffened EOS with Young–Laplace are in near-quantitative agreement with values calculated in simulation. The approximation $(\partial P/\partial\rho)_S \approx (\partial P/\partial\rho)_T$ appears to hold well, and the two simulation methods agree that $c^2 < 0$ in the bubbly region, while $c^2 > 0$ for homogeneously stretched water (Fig. 5).

The inclusion of nitrogen at a mole fraction of 0.001 (80 times greater than the equilibrium mole fraction in the liquid phase at 0.1 MPa[27,41]) alongside mW water at edge length L = 8 nm and

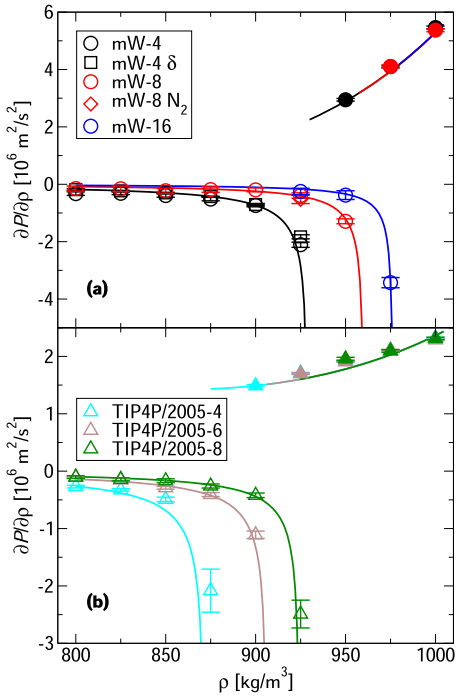

FIG. 5. Speed of sound measurements from molecular simulation (symbols) overlaid with the EOS with Young–Laplace predictions at constant V (solid lines) using the (a) mW and (b) TIP4P/2005 water models. Finite size effects are illustrated with different colors: black, red, and blue for mW sizes L = 4, 8, and 16 nm, and cyan, brown, and green for TIP4P/2005 sizes L = 4, 6, and 8 nm, respectively. Simulation results are for single-component (water only) simulations except for the diamond marker at mW L = 8 nm and ρ = 925 kg/m^3, which included nitrogen at a mole fraction of 0.001. Simulation results were measured using the direct thermodynamic approach of Lustig,[32] giving $(\partial P/\partial\rho)_S$ except for the square markers also shown for the mW L = 4 nm system, which were measured using finite differences and give $(\partial P/\partial\rho)_T$.

22 November 2024 13:32:09

Published under an exclusive license by AIP Publishing

density $\rho = 925$ kg/m^3 makes a near-negligible change to the measurement of c^2, which remains <0. This is in agreement with the pressure–density data from Chen *et al.*,[11] as seen in Fig. 1.

In the homogeneously stretched case, estimates for c^2 are independent of L for each model, as is to be expected from prior works. In the bubbly region, $|c^2| \to 0$ both as L increases at fixed ρ and as a function of decreasing ρ at fixed L. Both of these behaviors are in line with prior observations.[11] This data cumulatively illustrates the robustness of the observation that $\partial P/\partial \rho < 0$ in bubbly water systems and that it is more pronounced for smaller system sizes.

Comparisons involving the bubble volume between simulation and the stiffened EOS with Young–Laplace are complicated by a degree of arbitrariness in selecting a bubble detection method in molecular simulations. Figure 6(a) shows a comparison between the bubble volume fraction α as a function of density for the EOS (solid line) and from simulation, using two different bubble detection methods: a voxel-based approach as described in Chen *et al.*[11] and the mesh-based Willard–Chandler approach[28] as described herein. The EOS result tends to overpredict the bubble volume compared to the simulation results for both detection methods. This may be attributed to the fact that the stiffened EOS with Young–Laplace considers the vapor–liquid interface to be infinitesimally thin, occupying zero volume, while simulation results have demonstrated that the interfacial region is several Å thick.[11]

From finite differences, $(\partial V_\alpha/\partial V)_N$ is accessible from molecular simulations via fitting, as was done for $(\partial P/\partial \rho)_T$. In agreement with the stiffened EOS with Young–Laplace prediction, $\partial V_\alpha/\partial V > 1$ for both water models across the entire span of considered densities when the mesh-based bubble detection method is used (Fig. 6). Despite quantitative discrepancies, the important physics being captured is that $\partial V_\alpha/\partial V > 0$ is a thermodynamic requirement for $\partial P/\partial V < 0$, and both of these inequalities have been shown to hold. The voxel-based bubble detection method considers only voxels with vapor-like densities and does not yield $\partial V_\alpha/\partial V > 1$ for larger bubbles. The mesh-based method, which places an isosurface at approximately one half of the bulk liquid density, is in closer agreement with the EOS and agreement improves for larger system sizes. Discrepancies between the stiffened EOS with Young–Laplace and simulation results can also be attributed to a difference in path. Here, $(\partial V_\alpha/\partial V)_N$ is estimated at various ρ from simulations carried out at constant V but with different N. The inequality $\partial V_\alpha/\partial V > 1$ may not strictly hold when the constant N path is not followed.

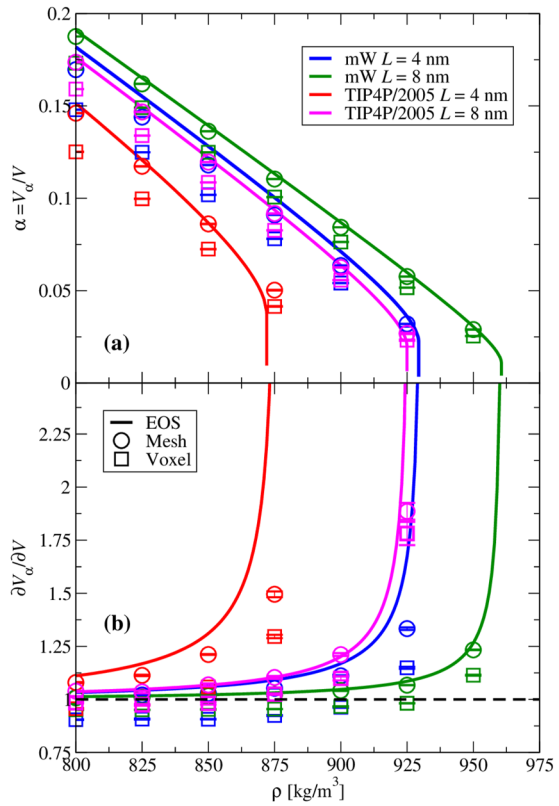

FIG. 6. (a) Comparison of two bubble detection methods in molecular simulation (symbols) against the prediction from the stiffened EOS with Young–Laplace at constant N (solid line), as a function of total density ρ (circular symbols: mesh-based, as described in the main text, and square symbols: voxel-based, as in Chen *et al.*[11]). The mW water model is represented in blue and green, while TIP4P-2005 is in red and magenta for the respective system sizes $L = 4$ and 8 nm. (b) The derivative $\partial V_\alpha/\partial V$ computed via finite differences from simulations and compared against the EOS. Note that the EOS is generated in an ensemble at constant N while simulation data were gathered at constant V. Symbols and colors are the same in the two panels.

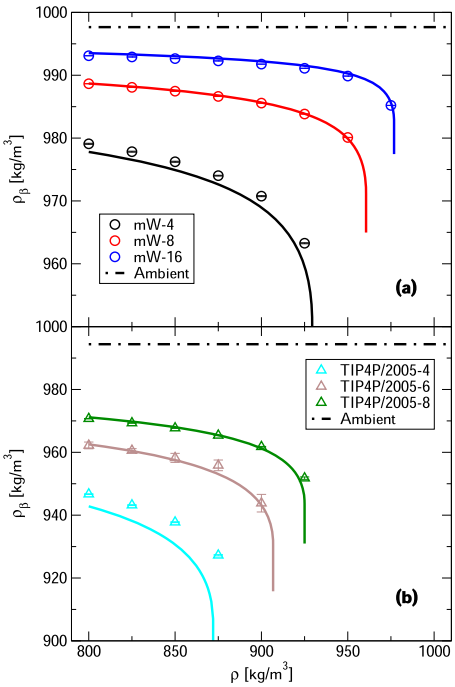

FIG. 7. Comparison between numerical results using the stiffened EOS with Young–Laplace at constant V (lines) with molecular simulation results as described herein (symbols) for two water models: (a) mW and (b) TIP4P/2005. Parameters for the stiffened EOS were fit from the homogeneous simulation data. A horizontal dashed black line indicates the saturated liquid density of the water model at ambient conditions. Different symbol colors indicate simulations of different sizes, where the number that appears in the legend is the simulation box edge length L, in nm.

22 November 2024 13:32:09

Published under an exclusive license by AIP Publishing

The density of the liquid phase, ρ_β, similarly shows near-quantitative agreement with the stiffened EOS with Young-Laplace at large V (Fig. 7). For small system sizes, the EOS slightly underpredicts the liquid density, which is attributed to a slightly larger effective volume of the liquid region when the contribution of the interface is neglected. The derivative $\partial\rho_\beta/\partial\rho$ is clearly negative in all cases, for a variety of system sizes and both water models. This is the necessary condition for $\partial P/\partial\rho_\beta > 0$ for sound propagation.

The behaviors of V_α and ρ_β can be used to explain the step change that occurs in $\partial P/\partial\rho$ near the spinodal decomposition point (Fig. 5). As noted earlier, pressure changes are largely driven by relaxation in the surrounding liquid. This increase in the liquid density is particularly sharp near the spinodal decomposition point because the bubble volume rises sharply from zero (in the homogeneously stretched liquid) as the bubble first forms. Quantitatively, these behaviors are seen in Figs. 6(a) and 7, respectively. The bubble volume undergoes what is essentially a step change at the point of bubble formation, which is attributed to sub-nanometer scale bubbles being unstable in the face of thermal fluctuations in the surrounding liquid. The emergence of a bubble is abrupt, leading to a jump in the liquid density, the pressure, and the compressibility over small changes in system density.

Determining $c_\beta \equiv (\partial P/\partial\rho_\beta)^{1/2}$ via finite differences is more challenging than measuring $\partial P/\partial\rho$ because both P and ρ_β are subject to uncertainties, which are exacerbated during the fitting process.

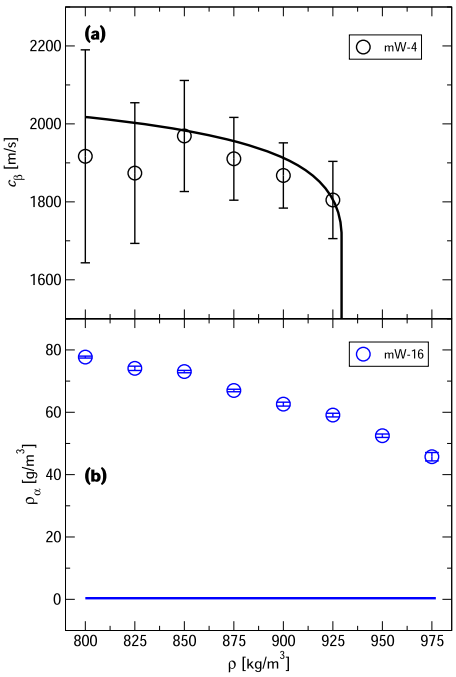

FIG. 8. (a) The liquid speed of sound, c_β, for the mW water model at system size $L = 4$ nm and (b) the vapor density ρ_α for the mW water model and $L = 16$ nm system as a function of system density, ρ, as determined from simulation (symbols) and the stiffened EOS with Young–Laplace at constant V (lines).

The resulting uncertainties in c_β from simulation are therefore relatively large, but the averages are unambiguously positive and of a comparable order of magnitude to the prediction from the stiffened EOS with Young-Laplace [Fig. 8(a)]. Data are only shown for the system with the highest statistical precision, mW $L = 4$ nm. Consistent agreement between simulation and numerical modeling suggests that the stiffened EOS with Young–Laplace is a viable predictor for some thermophysical properties of water without the computational expense of conducting molecular simulations.

The stiffened EOS with Young–Laplace assumed $\partial\rho_\alpha/\partial\rho = 0$, and we here address the validity of that assumption. The available simulation data taken from the largest system size studied (mW model and $L = 16$ nm) suggest that ρ_α decreases approximately linearly with increasing system density [Fig. 8(b)], but varies only by g/m^3 rather than kg/m^3 like the liquid. This is to say that, by comparison to ρ_β [Fig. 7(a)], ρ_α is relatively constant, and the assumption made in the stiffened EOS with Young–Laplace is well-justified despite being much larger than the bulk saturated vapor density. Thermodynamic arguments can explain the trend that ρ_α decreases as the overall system density rises because the stretched liquid phase surrounding the bubble has a lower chemical potential than the liquid at ambient conditions. At equilibrium, the vapor bubble and the surrounding liquid must have the same chemical potential, so μ_α rises (and thus ρ_α rises) as ρ_β relaxes. This is to say that $\partial\rho_\alpha/\partial\rho_\beta$ is >0.

With ρ_α varying only slightly, it is important to consider the ramifications of approximating it as constant. Taking ρ_α as a constant has profound consequences for the relationship between thermodynamic derivatives for the vapor phase. The usual Newton–Laplace equation $c^2 = K/\rho$ only holds for the entire system, where N is constant, and is invalid for each subsystem where the liquid and vapor can exchange particles. The Newton–Laplace equation arises from the equivalence,

$$-V\frac{\partial P}{\partial V} = \rho\frac{\partial P}{\partial \rho}. \tag{33}$$

A careful verification of this relation reveals the presence of a $\partial N/\partial V$ term that is usually unnecessary:

$$-V\frac{\partial P}{\partial V} = \left[\rho - \frac{\partial N}{\partial V}\right]\frac{\partial P}{\partial \rho}.$$

For either an isothermal or an adiabatic approach, N is constant and the derivative $\partial N/\partial V = 0$, returning Eq. (33). No such restriction exists on N_α or N_β, however. This has ramifications if the density of one phase remains constant. That is, for

$$-V_\alpha\frac{\partial P}{\partial V_\alpha} = \left[\rho_\alpha - \frac{\partial N_\alpha}{\partial V_\alpha}\right]\frac{\partial P}{\partial \rho_\alpha}, \tag{34}$$

having a constant vapor density requires that $\partial N_\alpha/\partial V_\alpha = \rho_\alpha$, giving zero on the right-hand side and the vapor speed of sound $\partial P/\partial\rho_\alpha$ is undefined. The compressibility still exists, however, because V_α is not fixed, and it is negatively valued in agreement with prior statements about pressure and volume derivatives.

Acknowledging that $\partial N_\alpha/\partial\rho_\alpha$ is not strictly zero alleviates the undefined behavior of the right-hand side of Eq. (34) but the importance of particle exchange between phases is clear. An accurate

22 November 2024 13:32:09

Published under an exclusive license by AIP Publishing

description of sound propagation in bubbly water requires a careful consideration of the various thermodynamic derivatives that govern the process.

C. Scattering functions

For each model, mW and TIP4P/2005, three densities were selected at a system size of $L = 4$ nm: one near ρ_β^{sat} (1000 kg/m^3), one in the homogeneously stretched region (950 kg/m^3), and one bubbly (900 kg/m^3 for the mW model and 850 kg/m^3 for TIP4P/2005). The densities in the bubbly region differ for the two models because the bubbly region begins at different densities for each (see Fig. 1). In homogeneous systems, speed of sound peaks are known to appear in both $F(k,t)$ and $S(k,\omega)$.[36,37] At this system size, the smallest accessible wavevector is $k \approx 0.1570\text{Å}^{-1}$, and so extrapolation to zero wavevector is required to produce an estimate for c that agrees with other methods. However, at this small system size, we can compute scattering functions very accurately to determine whether such peaks arise when the presence of a bubble obscures the signal. We begin with the intermediate scattering function $F(k,t)$ (Fig. 9).

For both water models, $F(k,t)$ is qualitatively similar at homogeneous densities (1000 and 950 kg/m^3), decaying to zero over time with some oscillatory behavior. Density–density correlations decay more slowly in the homogeneously stretched region due to the more ice-like behavior of water at lower densities.[11,42] Where oscillations in $F(k,t)$ are most prominent, speed of sound peaks arise within $S(k,\omega)$.

In bubbly systems, $F(k,t)$ is dominated by relatively long time scale density–density correlations. It is well known that water molecules at a vapor–liquid interface experience reduced effective friction due to participating in fewer hydrogen bonds than bulk water, and so are comparatively more mobile.[43] This slow decorrelation in $F(k,t)$ is likely attributed to the bubble itself, where the bubble center of mass is relatively slow-moving due to the collective motion required for its drift.

At the smallest wavevector, $F(k,t)$ is nearly constant over 30 ps (Fig. S1). Because $\text{FT}[\exp(-a|t|)] = 2a/(a^2+\omega^2)$, we see that, when $F(k,t)$ decays slowly, the corresponding $S(k,\omega)$ has strong $1/\omega^2$ character, obscuring peaks that may arise in $S(k,\omega)$. This effect is exaggerated at small wavevectors, where the peaks occur at smaller values of ω. At larger k, $F(k,t)$ decays more quickly [as is seen in Eq. (31)] and peaks occur at higher ω, making peaks in $S(k,\omega)$ detectable.

Only for the mW model are peaks in $S(k,\omega)$ sharp enough to pick out as local maxima. It is noteworthy that these peaks can be clearly identified for the mW model at $\rho = 900$ kg/m^3 for all but the two smallest wavevectors, which is a clear signal of sound propagation in a system where $\partial P/\partial\rho < 0$. For the TIP4P/2005 model, $S(k,\omega)$ has stronger $1/\omega^2$ character and so the speed of sound peaks appears as shoulders, although their presence remains clear and so the argument for sound propagation remains intact. In these cases, c_β must be identified via fitting, however, and so we return to $F(k,t)$.

In the homogeneously stretched region, the fitting function Eq. (31) matches the entirety of $F(k,t)$ very accurately. When a bubble is present, however, a set of parameters that capture both the slow decay of $F(k,t)$ over long times and the oscillatory behavior at short times could not be identified. This is attributed to anomalous dispersion arising from the presence of a vapor–liquid interface. Because we seek to identify c, fitting to $F(k,t)$ was performed only over short times to accurately capture the oscillatory behavior. The fitting window extended ~1.5 wavelengths [i.e., 1.5 times the argument to the trigonometric functions in Eq. (31), $(c_{\text{est}}kt)$] where c_{est} is an estimate of the resulting c. Because the quality of the fit is dependent on the fitting window, c_{est} was adjusted by ~20% to collect a family of fitted

22 November 2024 13:32:09

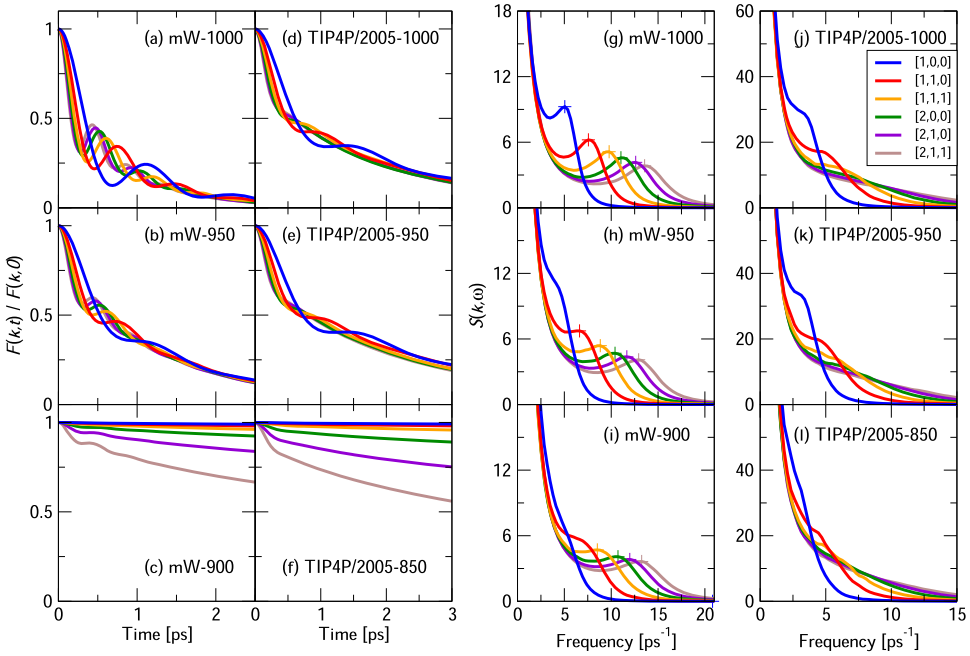

FIG. 9. Normalized intermediate scattering function $F(k,t)/F(k,0)$ for the mW model (first column) and the TIP4P/2005 model (second column) as well as dynamic structure factors $S(k,\omega)$ in units of fs for the mW model (third column) and TIP4P/2005 model (fourth column) at three densities: 1000 kg/m^3 (top row), 950 kg/m^3 (middle row), and 900 kg/m^3 for the mW model and 850 kg/m^3 for the TIP4P/2005 model (bottom row). Each panel is labeled with its model–density pairing, with the density in kg/m^3. The k-vectors are of the form $\mathbf{k} = (2\pi/L)[l,m,n]$ for integers l,m,n and the values of $[l,m,n]$ are indicated in the legend. Each panel contains traces for the six smallest magnitude wavevectors accessible.

Published under an exclusive license by AIP Publishing

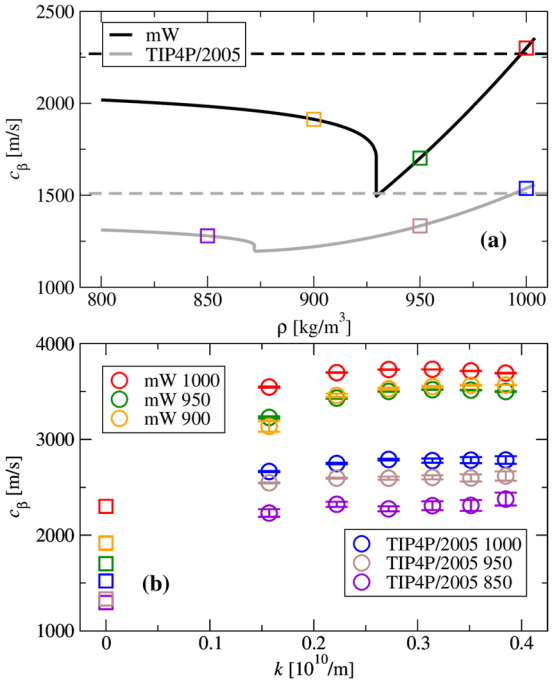

FIG. 10. (a) Numerical c_β from the stiffened EOS with Young–Laplace for both water models at a system size of $L = 4$ nm, with indicators (□) marking the densities chosen for scattering analysis, with each water model and density getting a different color. Dashed lines represent the values obtained for the liquid phase at the saturated vapor pressure.[11] (b) $c(k)$ fitted from simulated $F(k,t)$ data using Eq. (31) (○) and with corresponding points from panel (a) (□) as a reference at $k = 0$, using the same colors in both panels.

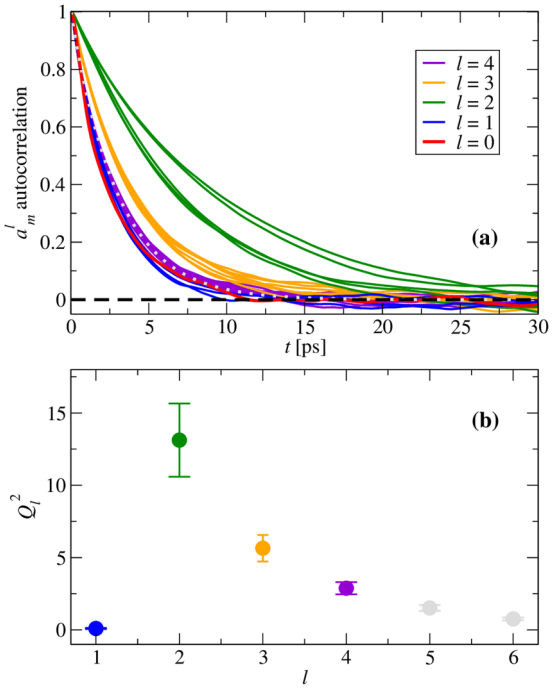

FIG. 11. (a) Autocorrelation function of the spherical harmonic basis function amplitudes, a_m^l, over time, color-coded by the order l (red: 0; blue: 1; green: 2; gold: 3; purple: 4). The asymptote at zero is given as a black dashed line, while a decaying exponential given by $\exp(-t/\tau)$ with $\tau = 3$ ps is in dotted gray. (b) The Steinhardt invariant Q_l^2 for each order l. The $l = 0$ spherical mode is two orders of magnitude greater than the others and is not shown for clarity.

c values and their average reported. The standard error of the mean is relatively small [Fig. 10(b)].

We find that fitted values for c deviate only slightly as a function of k, and differ between models and densities following the trends expected from the EOS in Fig. 10(a). While the extrapolation of fitted $c(k)$ to $c(0)$ is clearly in disagreement with the $k^{5/2}$ dependence of mode coupling theory,[37] the physical principle we seek to highlight is that real-valued sound modes can be identified in bubbly water systems, where $\partial P/\partial\rho < 0$, which are in good agreement with trends in homogeneous systems ($\partial P/\partial\rho > 0$).

D. Spherical harmonics

It is feasible that the sound attenuation properties of a bubble are related to a resonance of some spherical harmonic mode with propagating waves. When evaluated in simulation for the mW water model at a system size of $L = 4$ nm, the spherical harmonics mode amplitudes a_m^l that describe the bubble manifold display exponentially decaying time autocorrelation functions [Fig. 11(a)] with characteristic time constants ≥3 ps (dotted line). A time constant of comparable magnitude can be found by dividing the simulation box edge length L by the liquid speed of sound, c_β, which is ≈2 ps for the mW model. This is the recurrence time of a wave traveling unidirectionally through the simulation with a propagation direction along the lattice vector of the periodic simulation box. Notably, the a_m^l autocorrelation functions are monotonic and do not display recurrence peaks as one sees in $F(k,t)$.

The $l = 2$ modes show the slowest decay with a time constant of ≈10 ps. Modes other than $l = 2$ and $l = 3$ decay at approximately the same rate as the $l = 0$ spherical mode, showing correlation times on par with undulations in the bubble radius. It is not unusual for the $l = 2$ mode to stand out among the spherical harmonic degrees, as an $(l-1)$ term appears in expressions for the change in energy when a spherical droplet is perturbed.[44–46] The $l = 2$ mode is the lowest spherical harmonic order that can allow unbounded fluctuations. The Steinhardt invariant $Q_l^2 = \sum_{m=-l}^{l} a_{lm}^2$ is a sort of "power spectrum" of the spherical harmonic contributions, which quantifies the rotationally invariant contribution of the various l modes [Fig. 11(b)]. Indeed, the $l = 2$ mode has the largest contribution (aside from the radial $l = 0$) and has a characteristic time constant dissimilar to wave propagation.

IV. CONCLUSION

We have demonstrated through thermodynamic arguments that two-phase bubbly systems exhibit an unusual pressure–volume relation, $\partial P/\partial V > 0$, that occurs because the liquid becomes denser upon system expansion and the bubble grows by a greater increment than the system. This inequality remains true up to

22 November 2024 13:32:09

Published under an exclusive license by AIP Publishing

macroscopically resolvable bubbles on the millimeter scale, as quantified by a stiffened EOS with Young–Laplace. This numerical model further explains why experimental pressure measurements in bubbly water systems are positive, while nanoscale simulations predict negative pressure values, which is an effect of the system size. Molecular simulations calculating directly the speed of sound agree quantitatively with the EOS, demonstrating that $\partial P/\partial \rho$ is not a strictly positive quantity as is the case in homogeneous systems.

This finding can be reconciled with observations of sound propagation in bubbly systems by recognizing that the corresponding pressure derivative with the liquid density (rather than the total density) provides a positive value. This liquid sound speed is found to approach that of bulk water as the liquid density relaxes and is well captured by the stiffened EOS with Young–Laplace across a range of system densities. Sound propagation can be further identified in molecular simulations of bubbly water, where scattering functions contain characteristic speed-of-sound peaks. These peaks are partially obscured by long-lived density–density correlations associated with the bubble but can be identified via fitting. The spherical harmonic modes of the bubble envelope were not found to resonate on time scales commensurate with the speed of sound. While the conclusions given likely hold for a window of temperatures surrounding 298 K, the upper and lower bounds, where breakdown occurs, are unknown and must be examined carefully.

The approximation that the vapor density remains relatively constant as a function of overall system density appears well-justified. The corresponding pressure derivative is therefore sensitive, although the vapor compressibility is real-valued and negative. This challenges the theoretical foundations of commonly used equations describing sound speed c as a function of bubble fraction α, despite their apparent success in predicting experimental results. The discrepancy arises from the fact that the compressibility of water vapor as a homogeneous system is different from that of water vapor confined within a bubble. Further research will be required to quantitatively link the $\partial P/\partial \rho < 0$ detailed here and the experimentally observed real-valued c that is known to be sensitive to bubble void fraction by developing relations to quantify particle exchanges between phases.

SUPPLEMENTARY MATERIAL

The supplementary material for this article includes a PDF file containing the volume derivatives of the mW potential energy function needed to compute the speed of sound, plots of $F(k,t)$ in bubbly systems out to large t, and simulation results in tabular form.

ACKNOWLEDGMENTS

This work was supported by the Unites States Office of Naval Research under Grant No. ONR N00014-17-1-2676 with Dr. Ki-Han Kim and Dr. Yin-Lu Young as the program managers. Part of the computer resources was provided by the Minnesota Supercomputing Institute.

AUTHOR DECLARATIONS

Conflict of Interest

The authors have no conflicts to disclose.

Author Contributions

Jesse L. Prelesnik: Conceptualization (equal); Data curation (lead); Formal analysis (equal); Methodology (equal); Validation (lead); Visualization (lead); Writing – original draft (lead); Writing – review & editing (equal). **Jingyi L. Chen**: Conceptualization (equal); Formal analysis (equal); Investigation (equal); Writing – review & editing (equal). **Krishnan Mahesh**: Conceptualization (equal); Funding acquisition (lead); Supervision (equal); Writing – review & editing (equal). **J. Ilja Siepmann**: Conceptualization (lead); Formal analysis (equal); Funding acquisition (equal); Methodology (equal); Supervision (lead); Writing – review & editing (equal).

DATA AVAILABILITY

The data that support the findings of this study are available within the article and its supplementary material.

REFERENCES

[1] X. W. Luo, B. Ji, and Y. Tsujimoto, "A review of cavitation in hydraulic machinery," J. Hydrodyn. **28**, 335–358 (2016).
[2] M. Bhatt and K. Mahesh, "A numerical approach to address the acoustic stiffness in cavitating flows," Int. J. Multiphase Flow **141**, 103568 (2021).
[3] K. Schmidmayer, S. H. Bryngelson, and T. Colonius, "An assessment of multicomponent flow models and interface capturing schemes for spherical bubble dynamics," J. Comput. Phys. **402**, 109080 (2020).
[4] G. Yadigaroglu and G. F. Hewitt, *Introduction to Multiphase Flow: Basic Concepts, Applications and Modelling* (Springer, Cham, 2017).
[5] C. T. Crowe, *Multiphase Flow Handbook* (CRC Press, Boca Raton, 2005).
[6] V. E. Nakoryakov, B. G. Pokusaev, and I. R. Shreiber, *Wave Propagation in Gas-Liquid Media* (CRC Press, Boca Raton, 1993).
[7] P. S. Epstein, *Textbook of Thermodynamics* (John Wiley & Sons, New York, 1937).
[8] A. Sommerfeld, *Thermodynamics and Statistical Mechanics* (Academic Press, London, 1964), Vol. 5.
[9] D. Lee, M. Telo da Gama, and K. Gubbins, "A microscopic theory for spherical interfaces: Liquid drops in the canonical ensemble," J. Chem. Phys. **85**, 490–499 (1986).
[10] K. Binder, "Theory of first-order phase transitions," Rep. Prog. Phys. **50**, 783 (1987).
[11] J. L. Chen, B. Xue, K. Mahesh, and J. I. Siepmann, "Molecular simulations probing the thermophysical properties of homogeneously stretched and bubbly water systems," J. Chem. Eng. Data **64**, 3755–3771 (2019).
[12] F. B. Jensen, W. A. Kuperman, M. B. Porter, H. Schmidt, and A. Tolstoy, *Computational Ocean Acoustics*, 2nd ed. (Springer, New York, 2011).
[13] L. D. Landau and E. M. Lifshitz, *Statistical Physics* (Pergamon Press, Oxford, 1959), Vol. 5.
[14] A. J.-M. Yang, "The thermodynamical stability of the heterogeneous system with a spherical interface," J. Chem. Phys. **82**, 2082–2085 (1985).
[15] P. Montero de Hijes and C. Vega, "On the thermodynamics of curved interfaces and the nucleation of hard spheres in a finite system," J. Chem. Phys. **156**, 014505 (2022).
[16] A. J.-M. Yang, "Free energy for the heterogeneous systems with spherical interfaces," J. Chem. Phys. **79**, 6289–6293 (1983).

22 November 2024 13:32:09

Published under an exclusive license by AIP Publishing

[17]I. Sanchez-Burgos, M. C. Muniz, J. R. Espinosa, and A. Z. Panagiotopoulos, "A deep potential model for liquid–vapor equilibrium and cavitation rates of water," J. Chem. Phys. **158**, 184504 (2023).
[18]K. Davitt, E. Rolley, F. Caupin, A. Arvengas, and S. Balibar, "Equation of state of water under negative pressure," J. Chem. Phys. **133**, 174507 (2010).
[19]M. Tanaka, G. Girard, R. Davis, A. Peuto, and N. Bignell, "Recommended table for the density of water between 0 °C and 40 °C based on recent experimental reports," Metrologia **38**, 301–309 (2001).
[20]W. Wagner and A. Pruß, "The IAPWS formulation 1995 for the thermodynamic properties of ordinary water substance for general and scientific use," J. Phys. Chem. Ref. Data **31**, 387–535 (2002).
[21]T. Petrova and R. B. Dooley, "Revised release on surface tension of ordinary water substance," The International Association for the Properties of Water and Steam, Release R1-76 (2014), see https://www.iapws.org/relguide/Surf-H2O.html.
[22]D. R. Lide, *CRC Handbook of Chemistry and Physics* (CRC Press, Boca Raton, 2004), Vol. 85.
[23]J. L. Abascal and C. Vega, "A general purpose model for the condensed phases of water: TIP4P/2005," J. Chem. Phys. **123**, 234505 (2005).
[24]V. Molinero and E. B. Moore, "Water modeled as an intermediate element between carbon and silicon," J. Phys. Chem. B **113**, 4008–4016 (2009).
[25]S. Deublein, B. Eckl, J. Stoll, S. V. Lishchuk, G. Guevara-Carrion, C. W. Glass, T. Merker, M. Bernreuther, H. Hasse, and J. Vrabec, "*ms2*: A molecular simulation tool for thermodynamic properties," Comput. Phys. Commun. **182**, 2350–2367 (2011).
[26]A. P. Thompson, H. M. Aktulga, R. Berger, D. S. Bolintineanu, W. M. Brown, P. S. Crozier, P. J. In't Veld, A. Kohlmeyer, S. G. Moore, T. D. Nguyen *et al.*, "LAMMPS: A flexible simulation tool for particle-based materials modeling at the atomic, meso, and continuum scales," Comput. Phys. Commun. **271**, 108171 (2022).
[27]J. L. Chen, J. L. Prelesnik, B. Liang, Y. Sun, M. Bhatt, C. Knight, K. Mahesh, and J. I. Siepmann, "Large-scale molecular dynamics simulations of bubble collapse in water: Effects of system size, water model, and nitrogen," J. Chem. Phys. **159**, 224505 (2023).
[28]A. P. Willard and D. Chandler, "Instantaneous liquid interfaces," J. Phys. Chem. B **114**, 1954–1958 (2010).
[29]A. P. Willard and D. Chandler, "The molecular structure of the interface between water and a hydrophobic substrate is liquid-vapor like," J. Chem. Phys. **141**, 18C519 (2014).
[30]T. Lewiner, H. Lopes, A. W. Vieira, and G. Tavares, "Efficient implementation of marching cubes' cases with topological guarantees," J. Graphics Tools **8**, 1–15 (2003).
[31]C. Zhang and T. Chen, "Efficient feature extraction for 2D/3D objects in mesh representation," in *Proceedings of 2001 International Conference on Image Processing (Cat. No. 01CH37205)* (IEEE, 2001), Vol. 3, pp. 935–938.
[32]R. Lustig, "Direct molecular *NVT* simulation of the isobaric heat capacity, speed of sound and Joule–Thomson coefficient," Mol. Simul. **37**, 457–465 (2011).
[33]R. Lustig, "Statistical analogues for fundamental equation of state derivatives," Mol. Phys. **110**, 3041–3052 (2012).
[34]J. S. Rowlinson and F. L. Swinton, *Liquids and Liquid Mixtures: Butterworths Monographs in Chemistry*, 3rd ed. (Butterworth-Heinemann, London, 1982).
[35]E. Fransson, M. Slabanja, P. Erhart, and G. Wahnström, "DYNASOR: A tool for extracting dynamical structure factors and current correlation functions from molecular dynamics simulations," Adv. Theory Simul. **4**, 2000240 (2021).
[36]J. Salacuse and P. Egelstaff, "Finite-size effects in molecular dynamics simulations: Intermediate scattering function and velocity of sound. III. Theory and application to a model krypton fluid," Phys. Rev. E **64**, 051201 (2001).
[37]M. Schoen, R. Vogelsang, and C. Hoheisel, "Computation and analysis of the dynamic structure factor $S(k, \omega)$ for small wave vectors: A molecular dynamics study for a Lennard-Jones liquid," Mol. Phys. **57**, 445–471 (1986).
[38]I. De Schepper, J. Van Rijs, A. Van Well, P. Verkerk, L. De Graaf, and C. Bruin, "Microscopic sound waves in dense Lennard-Jones fluids," Phys. Rev. A **29**, 1602 (1984).
[39]C. R. Nortje, W. O. Ward, B. P. Neuman, L. Bai *et al.*, "Spherical harmonics for surface parametrisation and remeshing," Math. Probl. Eng. **2015**, 582870.
[40]E. W. Lemmon, *Thermophysical Properties of Fluid Systems* (National Institute of Standards and Technology, MD, 2010).
[41]T. R. Rettich, R. Battino, and E. Wilhelm, "Solubility of gases in liquids. XVI. Henry's law coefficients for nitrogen in water at 5 to 50°C," J. Solution Chem. **13**, 335–348 (1984).
[42]C. Marcolli, "Ice nucleation triggered by negative pressure," Sci. Rep. **7**, 16634 (2017).
[43]P. Liu, E. Harder, and B. Berne, "On the calculation of diffusion coefficients in confined fluids and interfaces with an application to the liquid–vapor interface of water," J. Phys. Chem. B **108**, 6595–6602 (2004).
[44]M. I. Oh, A. Malevanets, M. Paliy, D. Frenkel, and S. Consta, "When droplets become stars: Charged dielectric droplets beyond the Rayleigh limit," Soft Matter **13**, 8781–8795 (2017).
[45]A. Malevanets, M. I. Oh, M. Sharawy, and S. Consta, "Landau–Ginzburg theory for 'star'-shaped droplets," Mol. Phys. **116**, 2892–2900 (2018).
[46]S. Consta and A. Malevanets, "Disintegration mechanisms of charged nanodroplets: Novel systems for applying methods of activated processes," Mol. Simul. **41**, 73–85 (2015).

22 November 2024 13:32:09

Published under an exclusive license by AIP Publishing